

Computational Time Reversal for NDT Applications Using Experimental Data

Lopatin, Craig; Rabinovich, Daniel; Givoli, Dan; Turkel, Eli

DOI

[10.1007/s10921-017-0424-6](https://doi.org/10.1007/s10921-017-0424-6)

Publication date

2017

Document Version

Final published version

Published in

Journal of Nondestructive Evaluation

Citation (APA)

Lopatin, C., Rabinovich, D., Givoli, D., & Turkel, E. (2017). Computational Time Reversal for NDT Applications Using Experimental Data. *Journal of Nondestructive Evaluation*, 36(3), Article 48. <https://doi.org/10.1007/s10921-017-0424-6>

Important note

To cite this publication, please use the final published version (if applicable). Please check the document version above.

Copyright

Other than for strictly personal use, it is not permitted to download, forward or distribute the text or part of it, without the consent of the author(s) and/or copyright holder(s), unless the work is under an open content license such as Creative Commons.

Takedown policy

Please contact us and provide details if you believe this document breaches copyrights. We will remove access to the work immediately and investigate your claim.

Computational Time Reversal for NDT Applications Using Experimental Data

Craig Lopatin¹ · Daniel Rabinovich¹ · Dan Givoli^{1,2} · Eli Turkel³

Received: 11 November 2016 / Accepted: 23 May 2017
© Springer Science+Business Media New York 2017

Abstract A model-based non destructive testing (NDT) method is proposed for damage identification in elastic structures, incorporating computational time reversal (TR) analysis. Identification is performed by advancing elastic wave signals, measured at discrete sensor locations, backward in time. In contrast to a previous study, which was purely numerical and employed only synthesized data, here an experimental system with displacement sensors is used to provide physical measurements at the sensor locations. The performance of the system is demonstrated by considering two problems of a thin metal plate in a plane stress state. The first problem, which represents passive damage identification, consists in finding the location of a small impact region from remote measurements. The second problem is the identification of the location of a square hole in the plate. The difficulties one encounters in applying this identification method and ways to overcome them are described. It is concluded that while this is a viable model-based identifica-

tion method, which may lead, after further development, to a practical NDT procedure, one must be careful when drawing conclusions about its performance based solely on numerical experiments with synthesized data.

Keywords Non destructive testing · Non destructive evaluation · Model based · Time reversal · Inverse problems · Finite elements

1 Introduction

Purely experimental non-destructive testing (NDT) systems have the capability to detect damage in structures. However, they usually do not provide detailed information on the damage parameters, such as exact location and size. Hence, in recent years computational methods have been combined with physical NDT to yield better identification e.g., the book [1] and the review papers [2,3].

The diagrams in Fig. 1 illustrate the differences between a purely experimental ultrasonic NDT system and a model-based one. In the former, the response signals, measured by the sensors, are compared with those of a healthy structure. When the difference between the two sets of signals is larger than a certain threshold, this indicates damage in the specimen. In a model-based NDT system, the measured response signals are compared to those generated by a computational model which assumes a candidate flaw. If the two sets of signals are close to each other (in some specified norm), this indicates that the candidate flaw assumed by the model is similar to the true one. However, if the signals differ greatly this means that the candidate flaw has to be replaced by a better candidate. This leads to an optimization problem: Find the model's damage parameters that minimize the distance

✉ Daniel Rabinovich
aedaniel@technion.ac.il

Craig Lopatin
craiglopatin11@gmail.com

Dan Givoli
givolid@technion.ac.il

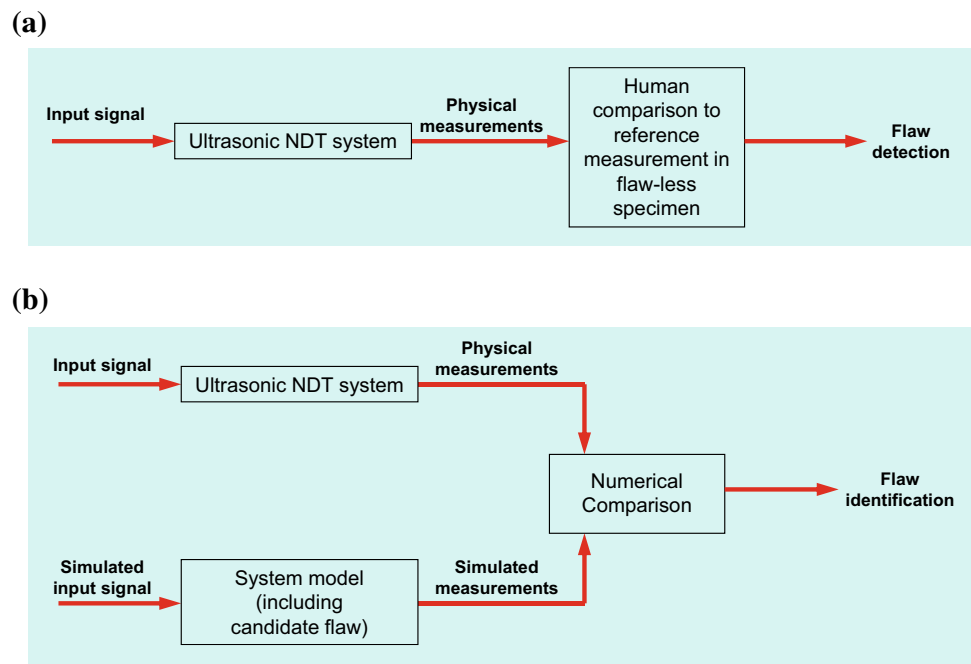
Eli Turkel
turkel@post.tau.ac.il

¹ Department of Aerospace Engineering, Technion — Israel Institute of Technology, 32000 Haifa, Israel

² Faculty of Civil Engineering & Geosciences, Technical University of Delft, 2600 GA Delft, The Netherlands

³ School of Mathematical Sciences, Tel-Aviv University, 69978 Tel Aviv, Israel

Fig. 1 **a** A purely experimental NDT system: flaw is detected based on comparing the measured signal with that of a flaw-less specimen. **b** A model-based NDT system: flaw is identified based on comparing the measured signal with a signal obtained by a computational model which assumes various candidate flaws



between the response signals measured and those computed by the model.

Note the terms “detection” and “identification” used in the purely experimental case and in the model-based case, respectively. *Detection* mainly answers the yes-or-no question: “is there a flaw in the structure?”, but provides little information beyond this. *Identification* seeks to find the detailed parameters of the flaw. Generally speaking, the more information obtained in this way on the flaw parameters, the higher the computational cost of this procedure.

From a mathematical perspective, damage identification is an inverse problem [4]. The computational part of a model-based ultrasonic NDT system thus involves the solution of an inverse wave problem [5–7]. Various computational methods have been devised to solve this problem. A direct optimization approach, called Full Waveform Inversion (especially in the geophysical literature) may be used to solve the minimization problem mentioned above, as in [8, 9]. If the objective function surface is smooth enough, a gradient-type minimization scheme may be employed. The adjoint method [8, 10, 11] can then be used to calculate the gradient of the objective function efficiently. A different class of solution methods is based on probabilistic analysis, as in [12]. Identification based on the spectrum (modal analysis) also constitutes an important class of methods; see, e.g., [13–16]. An alternative to these methods is the use of Arrival Time Imaging, also called Travel Time Migration or Kirchhoff Migration [17–19]. This is a fast but crude method, which is extremely popular in geophysical applications but less so in NDT applications.

Yet another class of computational methods of identification, which concerns us in the present study, is based on Time Reversal (TR). One should distinguish between physical TR, which is the original TR procedure invented by Fink et al. [20], and computational TR, which has been developed later; see the review paper [21]. It is the latter which concerns us in the context of model-based NDT. Computational TR has been applied to various NDT identification problems; see, e.g., [22–27]. Identification is performed by advancing wave signals, measured at discrete sensor locations, backward in time. The process is explained in detail in the next section.

Recently, a computational TR method was developed in the time domain for source and scatterer identification. This uses a procedure for incorporating multiple time measurements and a new optimization method for identifying scatterers [28–30]. This approach was applied to time-dependent acoustics in [28], using a finite element (FE) spatial discretization, and to elastodynamics in [29], using finite differences in space and time. In [30] a variant of the method was applied to the identification of cracks in membranes, whose behavior is governed by the scalar wave equation.

All computational identification methods, including TR, are based on data available by measurements taken at several points in space and (for time-dependent problems) in time. However, many of the papers mentioned above, including [28–30], do not involve a physical lab experiment to produce the data. *Instead, the data in these papers are generated numerically.* In the TR method, this is done by sampling

the solution of the corresponding forward problem, so as to produce a set of “measurements” at chosen points in space and time, and possibly adding random noise to these “measurements”. While this procedure is legitimate, and allows the development and verification of a computational identification method without the need for expensive and time consuming lab experiments, there is always a doubt whether the method would perform equally well with physical data instead of synthesized data. Indeed, the use of physical data introduces several difficulties that are not of concern in the purely numerical framework. We shall see that this is also true in the present study.

In the present paper we use the computational TR method in the context of NDT to identify certain features in a metal elastic plate. Mathematically, the inverse problem to be solved is governed by the equations of linear 2D elastodynamics. In contrast to [28–30], which was purely numerical and employed only synthesized data, now an experimental system with displacement sensors is used to provide physical measurements at the sensor locations. We demonstrate the performance of the system by considering two problems involving a thin metal plate in a plane stress state. The first problem is that of identifying, based on remote measurements, a small region impacted by a stiff object (a small ball). This represents passive damage identification, e.g., from a bird striking an aircraft body. The word “passive” is used to indicate that identification does not rely on a user-applied wave source, but on an uncontrolled source which may be the cause of damage. The goal is to identify the location and general size of the impact region. The second problem is the identification of the location of a square hole in the plate. This is an active identification problem, since in this case the wave source (which is still generated by an impact of a small object) is known and controlled.

We describe the difficulties we encountered in applying the proposed identification method and ways to overcome them. The main message arising from this study is that while the proposed method is a viable identification procedure which may lead, after further development, to a practical NDT method, one must be careful when drawing conclusions about its performance based solely on numerical experiments with synthesized data. We believe that this message is also relevant to other available model-based NDT methods.

Following is the outline of the remainder of this paper. In the next section we briefly present the basics of the computational TR method for source and flaw identification in structures. In Sect. 3 we describe the experimental setup. In Sects. 4 and 5 we present examples of source and flaw identification, respectively, using lab acquired data. As part of this presentation we discuss the difficulties encountered. We end with concluding remarks in Sect. 6.

2 The Computational Time Reversal (TR) Method

2.1 Acquiring Data

The first step in the TR procedure (or any other identification method) is to acquire the data on which the identification relies. We shall do this in two ways, and compare between them. The first way is via a lab experiment, as will be described in Sect. 3. The second way is by generating the data numerically, which is described in this section.

We consider a FE model describing 2D elastic wave propagation in a thin plate. This model will serve us later for the TR identification process, but we can also use it to generate the data, as described below. We consider the equations of linear elastodynamics in the computational domain $\mathbf{x} \in \Omega$ and in the time interval $t \in [0, T]$. The forward problem consists in finding the displacement wave field $u_i(\mathbf{x}, t)$ given full information on the model. Namely, in the forward problem, which is just used to generate “measurement” data, the wave source and any flaw that the structure contains are fully known and represented by the model. We assume that the source is localized, namely has a support in a small region $\Omega_I \subset \Omega$. See Fig. 2.

The forward problem is given by:

$$\rho \ddot{u}_i = \sigma_{ij,j} + f_i, \quad \sigma_{ij} = C_{ijkl} \epsilon_{kl},$$

$$\epsilon_{ij} = \frac{1}{2}(u_{i,j} + u_{j,i}), \quad 0 \leq t \leq T, \quad \mathbf{x} \in \Omega, \tag{1a}$$

$$\mathcal{B}_{ij} u_j = 0 \quad \text{on } \partial\Omega, \tag{1b}$$

$$u_i(\mathbf{x}, 0) = \chi_I(\mathbf{x}) u_{i0}(\mathbf{x}), \quad \mathbf{x} \in \Omega, \tag{1c}$$

$$\dot{u}_i(\mathbf{x}, 0) = \chi_I(\mathbf{x}) v_{i0}(\mathbf{x}), \quad \mathbf{x} \in \Omega. \tag{1d}$$

Here, index notation with the summation convention is applied. A superposed dot denotes time differentiation, and a comma indicates partial differentiation. The u_i , ϵ_{ij} , σ_{ij} and C_{ijkl} are, respectively, the displacements, strains, stresses and elastic moduli. The \mathcal{B}_{ij} are linear homogeneous boundary operators, which represent the type of boundary

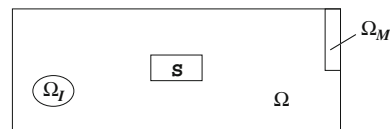


Fig. 2 Setup for the TR problem. Included in the domain Ω are the support of the initial conditions, Ω_I and the measurement domain Ω_M . Also shown is a scatterer (or damage region) S . In the source identification (refocusing) problem considered first, S is assumed to be known and Ω_I is unknown. In the scatterer identification problem, the source support Ω_I is known, whereas the S parameters are unknown

conditions applied in the experiment on the plate's boundary $\partial\Omega$, e.g., traction-free conditions. Also, f_i is the body force representing only the initially-applied force, if f_i is nonzero, then it is assumed that it has a short duration, and then it becomes zero. $\chi_I(\mathbf{x})$ is the characteristic function of Ω_I , defined by

$$\chi_I(\mathbf{x}) = \begin{cases} 1 & \text{if } \mathbf{x} \in \Omega_I, \\ 0 & \text{otherwise.} \end{cases} \quad (2)$$

Note that the "source" in this model is represented by either the initial body force peak, or the initial values u_{i0} and v_{i0} . If f_i is nonzero, u_{i0} and v_{i0} are assumed to equal zero, and vice versa.

We solve the forward problem (1) numerically, using FE discretization in space and explicit Newmark time integration [31], and we record the "measurements" during the simulation. These measurements are in general the Cauchy data u_i and $v_i = \dot{u}_i$ at the measurement times $t = t_m$, in the measurement region $\Omega_M \subset \Omega$; see Fig. 2. In practice, Ω_M is not a contiguous region but consists of discrete sensors. We add random noise to all these measurements, with a chosen intensity. Thus, we can write

$$\hat{u}_i(\mathbf{x}, t_m) = \chi_M(\mathbf{x}) (u(\mathbf{x}, t_m) + N_u(\mathbf{x}, t_m)) , \quad (3a)$$

$$\hat{v}_i(\mathbf{x}, t_m) = \chi_M(\mathbf{x}) (\dot{u}(\mathbf{x}, t_m) + N_v(\mathbf{x}, t_m)) , \quad (3b)$$

where N_u and N_v are random functions which represent measurement noise. The quantities on the left side of (3) constitute the synthesized data which the TR identification method relies on, if lab data are not used.

2.2 TR for Source Identification

Now, we consider the problem of source identification, which is related to passive damage identification. Namely, we assume that the region Ω_I is not known, and should be identified based on the measurements \hat{u}_i and \hat{v}_i in (3). Since the original source is local, and since we identify the source by letting waves evolve backward in time, the process is called *refocusing* [32]. Note that the goal is *not* to recover the source functions $u_0(\mathbf{x})$ and $v_0(\mathbf{x})$ themselves, but merely to find their support, i.e., the domain Ω_I .

We define the "reverse time" τ , which is related to t via the transformation

$$\tau = T - t . \quad (4)$$

Increasing τ from $\tau = 0$ means going backward in time, starting from $t = T$. We also define the "reverse field variable" $w(\mathbf{x}, \tau)$ for $\tau \in [0, T]$. The initial conditions for w are given from the measurements \hat{u}_i and \hat{v}_i we have at Ω_M for u at time $t = T$. Measurements at other times are superimposed on (i.e.,

added to) the solution during the backward time integration process. Note that if velocities measurements \hat{v}_i are available, they are taken *with the opposite sign*. This is implied by the fact that the velocities are the first time-derivatives of the displacements, so the transformation (4) reverses their sign, i.e., $\partial/\partial\tau = -\partial/\partial t$.

Other than that, the TR problem is similar to the forward problem. The governing equations (1a) are the same as in the forward problem, since these equations are invariant under the transformation (4). Note that in the TR problem the body force f_i is zero throughout. The same is true for standard boundary conditions (1b) which do not depend on time. Thus, the same FE code can be used to solve both the forward and TR problems.

We denote

$$\tilde{u}_0(\mathbf{x}) = w(\mathbf{x}, T) , \quad (5a)$$

$$\tilde{v}_0(\mathbf{x}) = -\dot{w}(\mathbf{x}, T) , \quad (5b)$$

which are the output of the problem. The functions \tilde{u}_0 and \tilde{v}_0 constitute the solution of the TR problem at time $\tau = T$, which corresponds to the forward time $t = 0$. As has been shown in [28], with a sufficient amount of measured data, excellent refocusing (or source identification) is achieved, namely the support of the functions \tilde{u}_0 and \tilde{v}_0 is approximately the true source support Ω_I .

2.3 TR for Flaw Identification

We now describe how TR can be used to identify a scatterer embedded in the computational domain, which is related to active damage identification. Again, we consider the setup of Fig. 2; however, now the parameters of the scatterer S are unknown, while the source support Ω_I is known.

The unknown scatterer is characterized by a set of parameters. The number and meaning of these parameters depend on the specific identification problem under study. Assuming, for simplicity, a single scatterer (a single damage region), the most general case is that where we know nothing about the scatterer location, size and shape. In the present work, we consider a scatterer in the form of a square hole in the plate, aligned with the directions of the plate edges. For simplicity, in the FE model we will assume that the hole has the correct shape and size, so that the only unknown parameters will be those associated with the *location* of the hole.

The scatterer identification is posed as an optimization problem: *Among all scatterer candidates, find the scatterer which yields the best wave refocusing at the true source location*. The proposed scatterer identification procedure can be described by the following steps:

1. Activate the source in the chosen location Ω_I , either by performing a lab experiment (as described in Sect. 3) or by solving numerically a “forward problem” (as described in Sect. 2.1). Record the response obtained at the sensor locations. If the data were generated numerically, add random noise to the measurements.
2. Assume a set of scatterer parameters, which represents one point in the space of candidate scatterers.
3. Based on the measured signals, perform a computational TR run, as described in Sect. 2.2, and obtain a solution at the reversed-time $\tau = T$.
4. Assess the quality of refocusing obtained at the original source Ω_I , by assigning a cost value \mathcal{C} to the candidate scatterer assumed in step 2.
5. Return to step 2, namely assume a new scatterer candidate, and continue the process, until a certain stopping criterion is met.
6. The minimal value of \mathcal{C} is hopefully attained by the correct set of scatterer parameters. The more prominent this minimum value is with respect to other cost values, the more confident we can be that this is the correct solution of the identification problem.

In the present case we wish to obtain a general overview picture of the cost function by enumerating fully *all* the possible locations of the flaw and the associated costs specifically in order to compare between the schemes using synthesized data and lab data. This picture is not affected by any special optimization techniques that in fact may be employed to find the actual minimum in a much faster way. A similar approach was presented in [30], albeit with a different cost function. That paper, as well as the present one, do not cover the choice and the use of a specific method of optimization, and the work presented here may serve as the basis for various possible extensions involving optimization. However, we comment that since the surface of the cost function is typically very ragged, a method of optimization that could be used for finding the minimum of the cost function in a more efficient way can not employ standard gradient-based or other conventional methods of optimization. Indeed, previous work carried out by us, see [34], demonstrates the usage of the metaheuristic optimization method of genetic algorithms for solving a not very dissimilar problem (employing the arrival time method rather than TR).

3 The Experimental Setup

The basic test configuration consisted of a rectangular plate, 1 cm thick, supported on top and bottom by soft rubber pads. Three configurations were used, with one configuration con-

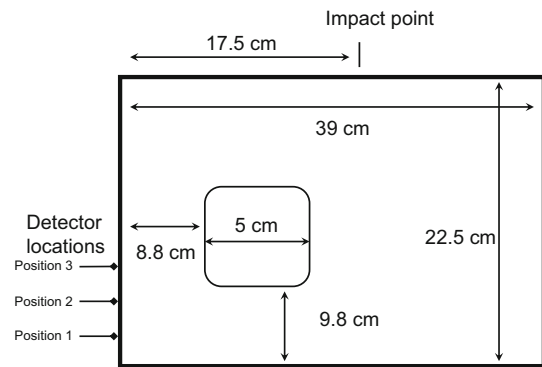


Fig. 3 Configuration 3

Table 1 The three configurations of tested plates

Configuration	Material	Defect
Configuration 1	Steel	No defect
Configuration 2	Aluminum	No defect
Configuration 3	Aluminum	5 cm square hole

taining a square hole, as shown in Fig. 3. The three variations are described in Table 1.

Waves were generated by dropping a 7 mm diameter steel ball onto the top surface at the indicated impact point. The normal displacement at the edge of the plate was measured using a Philtec optical displacement sensor (Type D20—with high frequency option). This sensor operates by illuminating the target surface with an optical fiber and detecting the amplitude of the reflected light. The amplitude versus distance to target calibration curve was provided by the manufacturer, and the sensors position was adjusted to be in the center of the linear, high sensitivity region (90 mV/micron). The frequency response of this type of displacement measurement method is determined by the electronics in this case, the frequency response of the sensor, as provided by the manufacturer, indicated a -3 dB point at 1 MHz, which was more than adequate for the experiments. The output from the displacement sensor was recorded using a Pico-Electronics digital oscilloscope, at a data acquisition rate of 0.2 ms per point. Typically, the displacement was detected at three different vertical locations, as indicated in Fig. 3, requiring three separate experiments. Figure 4 shows a photograph of the setup (with a smaller hole).

Figure 5 shows a typical displacement time history (the zero of the time axis is arbitrary, as pre-triggering was used). It is evident that the amplitude of the oscillations ranged from around a tenth of a micron to one micron. Also, there is a very low frequency component superposed on the oscillations, due to the rigid body motion of the plate.

In early experiments it was found that the size of the steel ball impactor had a significant effect on the frequency content of the waves impact with smaller balls resulted in oscillations

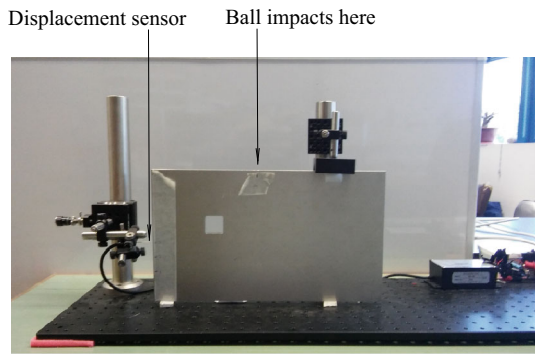


Fig. 4 Setup

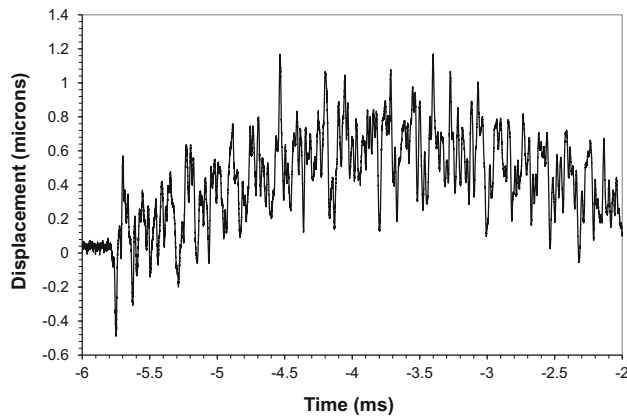


Fig. 5 Typical displacement time trace

with higher frequency content, and, as expected, with lower amplitude, compared to balls with larger diameters. Figure 6 shows this effect, comparing the responses of 10 and 7 mm balls. The arrows point to peaks observed using the 7 mm ball, but not observed using the 10 mm ball. While it is not clear why the ball diameter has such a significant effect on the wave structure, since the wave structure observed using the 7 mm ball best matches that predicted using the FE model (i.e. in the forward problem) the 7 mm ball was used for all the experiments reported here.

4 Source Identification: An Example

4.1 The Numerical Model

In the first example we wish to identify the impact source from the measurements taken at the three sensors. We use the finite element method (FEM) in order to model and simulate the behavior of the studied plates in the time-forward and the time-reversed runs. We construct a model of Configuration 1 (see Table 1) by considering a domain with the external dimensions given in Fig. 3, without the hole. The general tolerance between the numerical model and the experimental

setup shown in Fig. 3 was within 1.5 mm. A right-handed coordinate system was added to the rectangular domain in the numerical model, where the origin coincides with the southwestern corner of the plate and x -axis is aligned along the long side of the rectangle.

The domain was meshed with a structured mesh of square elements with a side length of 2.5 mm. Thus, the mesh corresponding to Configuration 1 contains 13950 elements. For the source identification example the 3 sensors were positioned at the following locations: Position 1 at (0, 0.05 m), Position 2 at (0, 0.1 m) and Position 3 at (0, 0.175 m). The sensors measure the x -displacements.

We assume that the medium is homogeneous, namely ρ and C_{ijkl} are constant throughout the plate model; and the elastic material is isotropic, namely

$$C_{ikjl} = \mu (\delta_{ij}\delta_{kl} + \delta_{il}\delta_{jk}) + \lambda \delta_{ik}\delta_{jl}, \tag{6}$$

where λ and μ are the Lamé constants, and δ_{ij} is the Kronecker delta.

We then make use of the assumption that the plate can be considered to be in *plane stress* state, according to which the Eq. (1) become two-dimensional (the indices i, j, k, l receive the only values 1, 2), and the elastic moduli C_{ijkl} in Eq. (6) are modified by changing the constants λ and μ :

$$\lambda = \frac{2\bar{\lambda}\bar{\mu}}{\bar{\lambda} + 2\bar{\mu}}; \quad \mu = \bar{\mu} \tag{7}$$

where $\bar{\lambda}$ and $\bar{\mu}$ are the actual material properties of the steel.

Although the plate rests on two supports, we will assume hereinafter that all the sides of the plate are traction-free. This does not introduce a large error, as the supports are much softer than the metal plate. The initial conditions at time 0^- (before the impact) are assumed to be zero displacement and zero velocity.

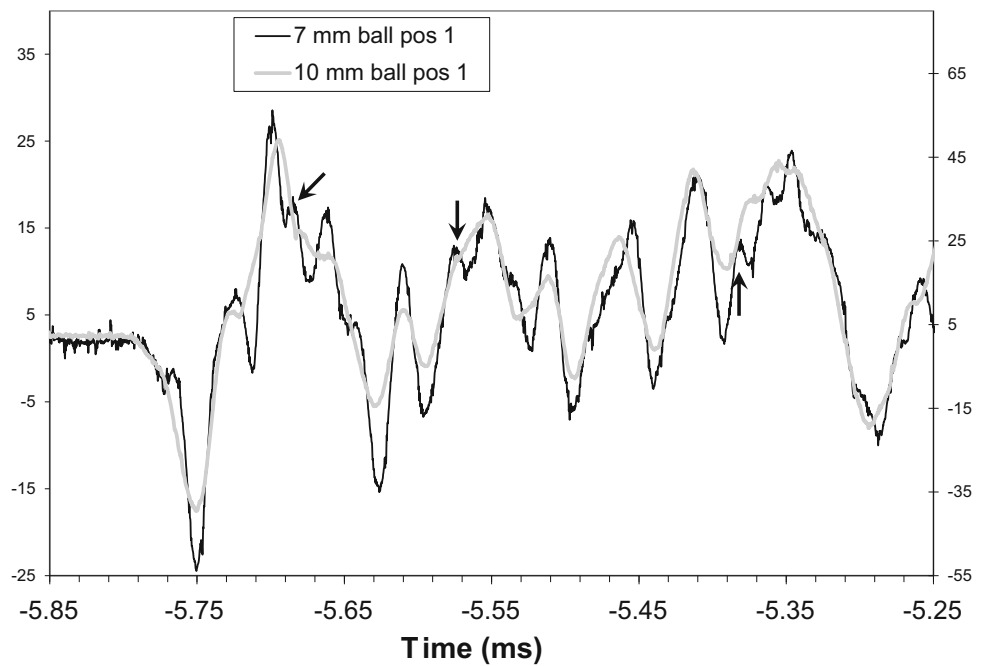
The source term of the signals due to the impact of the ball, f_i in (1a), can be represented by the following generalized function:

$$f_i = \frac{p_i(\mathbf{x})}{b} \delta(t) \tag{8}$$

where p_i are the components of the impulse per unit area applied to the plate by the ball, $\delta(t)$ is Dirac's delta function applied at the time $t = 0$, and $b = 1$ cm is the reference thickness dimension of the plate.

The distribution of impulse components p_i across the plate after impact can either be considered as concentrated at a single point, or localized in a small region about the point of impact. The initial distribution of the impulse governs the extent of high-frequency components in the numerical

Fig. 6 Comparison between the wave structure with 7 and 10 mm ball impactors



signals, in particular—at the sensors. We shall require that the initial impulse per unit area satisfy:

$$p_x \equiv 0, \tag{9}$$

$$\int_{\Omega} p_y d\Omega = \frac{I}{b}, \tag{10}$$

where Ω is the entire area of the plate, and I is the impulse imparted by the steel ball to the plate (the change in the ball’s momentum during the impact). If we choose to apply a point source, then we have $p_y = P\delta(x_0)$, where the force intensity P is such that (10) is satisfied, and x_0 is the impact point (0.1775, 0.225 m). Alternatively, with a slightly “smeared” source we choose the following expression for p_y :

$$p_x(x, y) = 0 \tag{11}$$

$$p_y(x, y) = A \cdot \begin{cases} 2\left(\frac{r}{a}\right)^3 - 3\left(\frac{r}{a}\right)^2 + 1 & \text{for } 0 \leq r \leq a \\ 0 & \text{otherwise} \end{cases} \tag{12}$$

The parameter a defines how localized the numerical source is, $r = \sqrt{(x - x_0)^2 + (y - y_0)^2}$, the factor A is a scaling parameter that governs the magnitude of the applied body force term. The impulse source chosen this way is C^1 -continuous.

As noted, the localization of the numerical model governs the extent to which high-frequency components are present in the generated signal. To illustrate this, consider the plots of the numerical signal measured at Position 1 for different values of a , as shown in Fig. 7. Note that the differences in

the displacement scale between the three graphs are due to the fact that different values of a represent different values of the total impulse imparted on the plate in the three tests.

For the linear problem the actual values achieved by the numerical and the experimental signals do not play any part in the identification processes described herein (the cost does not depend on A , see in the following sections), and one may scale the ordinates of these signals as one wishes without altering the identification performance. For this reason, the factor A can be chosen in an arbitrary manner.

4.2 The Numerical Algorithm

The spatial discretization of the problem was carried out using the standard Galerkin scheme, which yields the following semi-discrete set of equations for $t \geq 0^-$:

$$M\ddot{\mathbf{d}} + K\mathbf{d} = \mathbf{f}\delta(t) \tag{13}$$

$$\mathbf{d}(0^-) = \mathbf{0} \tag{14}$$

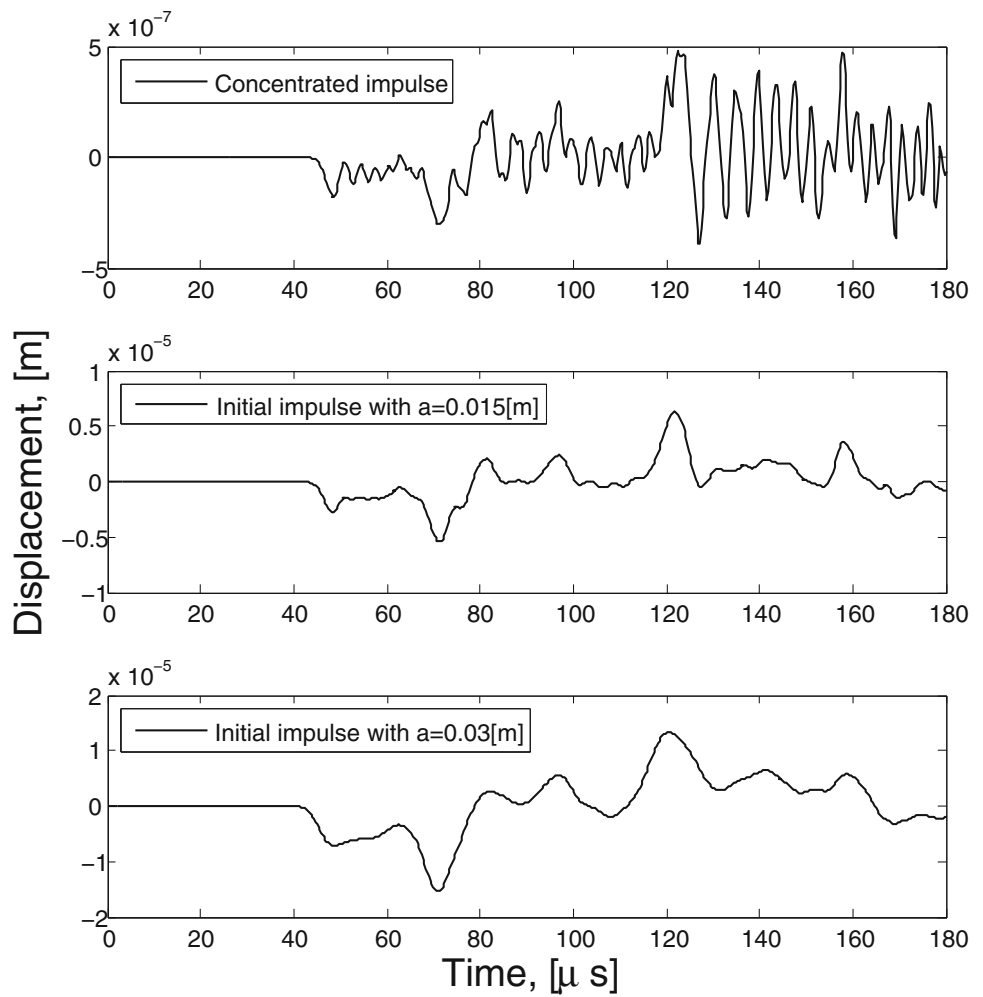
$$\dot{\mathbf{d}}(0^-) = \mathbf{0}, \tag{15}$$

where M and K are the mass and stiffness matrices, respectively, \mathbf{f} is the force vector, and \mathbf{d} is the vector of degrees of freedom of the model.

We integrate (13) in time from 0^- to 0^+ and obtain:

$$\int_{0^-}^{0^+} (M\ddot{\mathbf{d}} + K\mathbf{d}) dt = \mathbf{f} \int_{0^-}^{0^+} \delta(t) dt = \mathbf{f}, \tag{16}$$

Fig. 7 Comparison of the high frequency content at Position 1 for a with different localization



or

$$M (\dot{d}(0^+) - \dot{d}(0^-)) + K \int_{0^-}^{0^+} d dt = f. \tag{17}$$

The integral of d over a zero-length interval is $\mathbf{0}$. The remaining term gives:

$$M (\dot{d}(0^+) - \mathbf{0}) = f, \tag{18}$$

therefore (13)–(15) can be reformulated as:

$$M \ddot{d} + K d = \mathbf{0} \quad t > 0^+ \tag{19}$$

$$d(0^+) = \mathbf{0} \tag{20}$$

$$\dot{d}(0^+) = M^{-1} f. \tag{21}$$

The problem is therefore coded in such a manner that the source enters through the initial conditions, rather than the body force term.

We solve the problem using the second-order Newmark explicit algorithm, with $\beta = 0, \gamma = 0.5$. To select the time

step we require that the time step meet the CFL condition for stability. A time step of $\Delta t = 3 \times 10^{-7}$ s proved to be sufficient for all the runs performed.

4.3 Calibration of the Measurements

We carry out a tuning (calibration) procedure to match between the signal obtained from the experimental setup (see for example Fig. 5) of a particular configuration and the signal obtained from the forward solution of the numerical model with a similar configuration. We wish to linearly adjust the experimental signal in order to eliminate *a-priori* sources of discrepancy of the latter with the numerical signal. The following parameters are therefore tuned:

1. The material properties of the three experimental configurations are not precisely known in advance before the source identification tests are carried out, and therefore the properties of the numerical model are considered to be tunable parameters of the problem.

Since, as noted, the scaling of the displacement in (1a) is not crucial in the present case, we can set, for example, the density of the material to a fixed value (taken here as $\rho = 7850 \text{ kg/m}^3$ for the steel plate and $\rho = 2700 \text{ kg/m}^3$ for the aluminum plate), and optimize the elastic constants so that the best approximation is obtained between the numerical and the experimental signal waveforms. This is done as follows: After an initial guess of the values of the elastic constants, we perform an iterative one-dimensional search of the space spanned by the allowable values of the two independent elastic constants (the taxicab method, see for example [33]). This is carried out only once for Configuration 1 (steel plate) (and once for the aluminum plate in Configurations 2 and 3, see next section). This optimization loop is the external loop, and for each new guess of the elastic properties we then perform the geometric optimizations listed below.

2. We permit three types of linear transformations of the experimental graph in order to have this graph match the numerical one as closely as possible. In order to compare these signals, we make the linear adjustments detailed below to the initial segment of the experimental graph, in order to fit only that initial segment as closely as possible to the first 1000 time steps of the numerical graph. In these first 1000 time steps it is possible to adjust the shape of the experimental signal so that a close fit is obtained, while for longer times the numerical dispersion error becomes large and renders the attempt to fit the graphs impractical.

The three linear transformations applied (in the listed order) to the experimental signal are:

1. The first transformation is a shift of the vertical (displacement) axis. This allows us to calibrate the zero level of the signals at each of the sensors. Different vertical shifts are permitted in the signals from the three positions. The difference in vertical shift between the three sensor positions are due to low-frequency “noise” that has to be removed from the calculation.

Since the numerical graph begins at 0, the vertical shift of the experimental graph, u_s , equals the average value of that signal in the initial segment, before the signal from the impact reached the read position. We have $u^{ex} \rightarrow u^{ex} + u_s$, where u^{ex} is the experimental graph at each of the three sensors.

2. Shift of the horizontal (time) axis. An equal shift is permitted in the signals from the three positions. This accounts for the uncertainty concerning the precise moment the signal is felt by the sensors.

The time shift of the experimental graph was found simply by shifting all three experimental graphs relative to the numerical ones by the same extent $t \rightarrow t + t_s$, where

t is the time and t_s is the time shift, and finding the shift that gives the smallest norm with the best scaling (see next item).

3. Scaling of the vertical (displacement) axis. An equal scaling of the vertical axis is allowed in the signals from the 3 positions. The vertical scaling matching takes care of any errors in the factor transforming the measured voltage to the displacement, and any inaccuracies in the calculation of the momentum imparted by the ball.

The best scaling factor s , where we have $u^{ex} \rightarrow (u^{ex} + u_s) \cdot s$, was found for each time shift value as follows. We seek the scaling s of the graphs from all three positions, which minimizes the following L_2 norm:

$$\min_s \sqrt{\sum_{pos=1}^3 \sum_i (u_{num,i} - su_{exp,i})^2} \tag{22}$$

To find the minimum, we differentiate the sum under the square root by s and equate to 0:

$$-2 \sum_{pos=1}^3 \sum_i (u_{num,i} - su_{exp,i}) u_{exp,i} = 0, \tag{23}$$

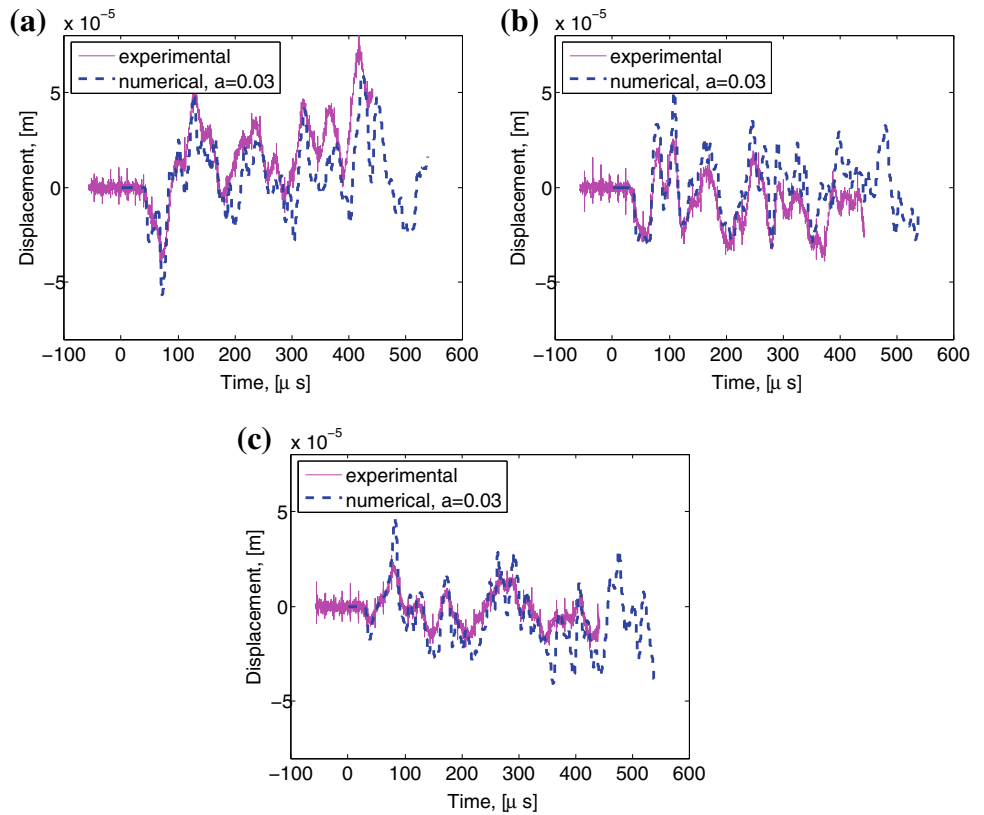
or,

$$s = \frac{\sum_{pos=1}^3 \sum_i u_{num,i} u_{exp,i}}{\sum_{pos=1}^3 \sum_i u_{exp,i}^2}. \tag{24}$$

Thus, Stage 1 was performed first, finding the vertical shift of each position. Subsequently, a time shift of 0 was set, and the appropriate vertical-axis scaling s was found from (24). Then, the time shift was repeatedly incremented by Δt^{ex} until the 1000-time step initial numerical segment went out of the entire experimental time range. For each particular time shift the scaling s was found, and the time shift and scaling corresponding to the best value of (22) overall were taken as the result of the optimization.

The optimized material properties obtained for Configuration 1 (steel) were $\bar{\mu} = 71 \text{ GPa}$, $\bar{\lambda} = 167 \text{ GPa}$, which give the plane stress values of $\mu = 71 \text{ GPa}$, $\lambda = 77 \text{ GPa}$. Shown in Fig. 8 is the comparison between the numerical signal and the transformed graph of the experimental signal as a function of time for the forward run using Configuration 1. One can see that initially there is agreement between the graphs, which becomes worse with time. This occurs mainly due to the expected accumulation of numerical error, but may also be affected by the measurement equipment. Whatever the source of the mismatch, it would make sense to only use approximately the first 600 time steps (180 μs) in the TR process.

Fig. 8 Configuration 1. Comparison of experimental and numerical data signals of the forward run: **a** Sensor position 1, scale transformation of the experimental graph: $t_{new}(\mu s) = t(\mu s) + 42.95$, $u_{new}(m) = (u(\text{Volt}) + 7.57) \cdot 2.9 \times 10^{-6}$; **b** Sensor position 2, scale transformation of the experimental graph: $t_{new}(\mu s) = t(\mu s) + 42.95$, $u_{new}(m) = (u(\text{Volt}) + 2.959) \times 2.9 \cdot 10^{-6}$; **c** Sensor position 3, scale transformation of the experimental graph: $t_{new}(\mu s) = t(\mu s) + 42.95$, $u_{new}(m) = (u(\text{Volt}) - 2.766) \times 2.9 \cdot 10^{-6}$; where t is the time and u is the displacement



4.4 Source Identification Procedure

Our goal is to identify the source by determining the approximate time and spatial location at which the impact was applied, by using the data obtained at the three measurement points. To this end we employ the method described above to time-reverse the measurement results—either the numerical ones or the physical ones.

In order to define the occurrence of identification following the time reversed run at the time T one needs to define what numerical quantity is expected to peak when the source is found, as well as characterize how “good” is that peak.

We considered several different fields that are expected to peak when a source is refocused:

1. The local energy, defined as: $E = \frac{1}{2}[\rho \dot{w}_i \dot{w}_i + \check{\sigma}_{ij} \check{\epsilon}_{ij}]$;
2. The magnitude of the displacement: $\sqrt{w_i w_i}$;
3. The squared y displacement w_y^2 .

The energy and squared y displacement fields were used in the present work for evaluating the quality of the time-reversed solution. The specific field used is indicated where applicable. One major criterion for the quality of the solution after the reversed run is that the peak occurs at the approximate location of the source (as the source is known). However, in the case of source identification the source is

not known to the investigator, and therefore a cost function has to be developed which would associate a cost with any given solution field, such that a low cost would correspond to good identification of the initial field (that occurred when the source was applied at the beginning of the forward run).

With this in mind, we choose for the present experiment the squared y displacement as the field on which we base the identification.

We first define the associated *Total Variation*:

$$TV(w_y) = \frac{h}{N_{np}} \sum_A \sqrt{(w_{y,x})^2 + (w_{y,y})^2}, \tag{25}$$

where h is the mesh parameter (element side length), N_{np} is the number of nodal points in the model, which serves as a normalization constant, A scans the nodal points. We use this definition in order to construct the following cost:

$$Cost_S = K_1 \frac{av(w_y^2(\Omega_{out}))}{max(w_y^2(\Omega))} + K_2 \frac{TV(w_y(\Omega_{out}))}{max(w_y^2(\Omega))}. \tag{26}$$

Here, K_1 and K_2 are constants, Ω_{out} is the domain of the problem which lies outside the square Ω_R (see Fig. 11c), which is defined as the square whose center coincides with the maximum of the peak (x_M, y_M) , such that $|x - x_M| \leq C_1$ and $|y - y_M| \leq C_1$ where C_1 is a constant which taken in the sequel as 7 element side lengths. Smaller values of

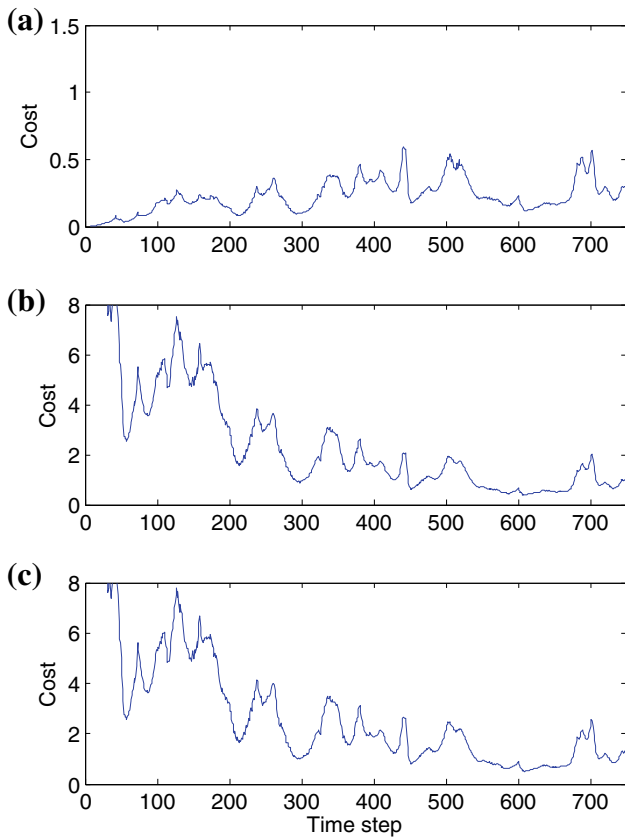


Fig. 9 The cost $Cost_S$ and its components for the numerically synthesized data. **a** Average component. **b** Total variation component. **c** $Cost_S$, sum of average and total variation components

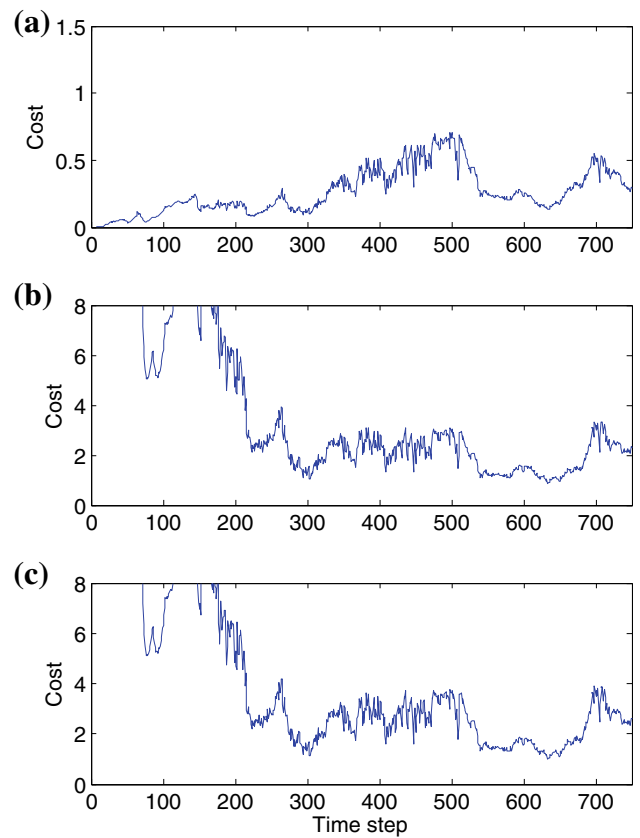


Fig. 10 The cost $Cost_S$ and its components for the experimental data. **a** Average component. **b** Total variation component. **c** $Cost_S$, sum of average and total variation components

C_1 were found to impair the performance of the method in identifying the source in some cases. The operator *av* stands for the average of the instantaneous field, and *max* stands for the maximum of this field.

The first term in (26) therefore assigns a high cost to solutions with a high average outside the main peak, which is expected to occur when there is a large number of high secondary peaks. The total variation term measures the deviation of such peaks from the average. The latter complements the former, as it will measure low “peakiness” when the average is high but even.

In addition to the exclusion of the Ω_R square for the calculation of the cost, we also exclude a strip $l_S = 8$ elements wide that is adjacent to the left boundary (the boundary on which the sensors are located) from Ω —we thus assume that the source is not located in this strip. Such an assumption is necessary since the sensors produce noise in the time-reversed run, which propagates mainly along this boundary. By masking using the specified strip the noise is eliminated.

We present the performance in terms of the cost $Cost_S$ of the numerically synthesized field and the experimental field, as these fields occur during the time-reversed stepping in Configuration 1. In each of the Figs. 9 and 10 we show plots of

the first component of $Cost_S$ (multiplied by the constant K_1), the second component (multiplied by the constant K_2), and the total cost, which is the sum of these components. Fig. 9 corresponds to the numerically synthesized input signals and Fig. 10 to the experimental signal. The goal of obtaining a minimum in the graphs in Figs. 9c and 10c at about the 600-th time step is not very sensitive to the precise values of K_1 and K_2 . The constants were selected manually as $K_1 = 8$ and $K_2 = 2 \cdot 10^{-8}$, which resulted in the performance described below.

It can be seen from Figs. 9 and 10 that with the selected K_1 and K_2 the cost component associated with the average of the field starts from 0 in both plots and gradually (though not monotonically) increases up to about the 500-th time step, after which it dips and then grows again at about the 700-th time step. The cost components associated with the total variation starts very large, decreases, and then exhibits a similar dip between the 500-th and 700-th time steps. The overall cost ($Cost_S$) is shown in subplot c) of Figs. 9 and 10. One sees that a minimum is attained at about the 600-th time step in both figures, which corresponds to the initial time in the forward run.

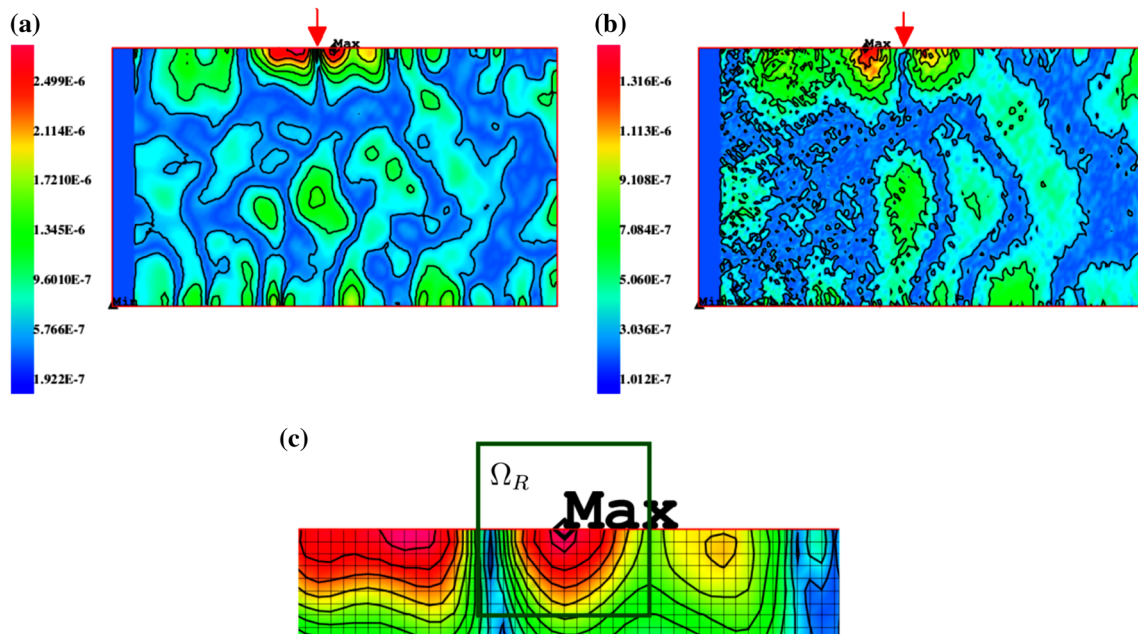


Fig. 11 Refocusing in $|w_y|$ field: **a** Numerically synthesized data; **b** Experimental data; **c** Fragment of **a** showing mesh and the square Ω_R

The total costs in subplots *c*) of Figs. 9 and 10 exhibit valleys with little change between time steps 550–650. This occurs since the refocused field travels in the vicinity of the true location at the upper boundary between these times. However, one should remember that the correct value of T is known to the user from determining the duration of the forward problem run. We therefore know what time to look at in Figs. 9 and 10, and show that a low cost is indeed obtained at these times. The fact that low costs are also obtained elsewhere as well (see Fig. 10c at about time step 300) does not interfere with the cost at T being low and therefore with its being regarded as identification of the source.

In order to see that refocusing does indeed occur when the described cost is low, we plot the $|w_y|$ field after the completion of the TR run (600 time steps), as shown in Fig. 11 for the case of the synthesized numerical signal and the experimental signal. In both cases there are prominent peaks at locations very close to that of the impact source. The impact point is marked with a red arrow.

One can see several differences in the features of the refocused field from the two sources: the field line in the numerical case are smoother due to the fact that the experimental are noisy; the highest peaks in both cases actually appear slightly to the right and to the left of the location of the true source, which can be explained by the fact that due to the accumulated error while stepping back in time the refocusing time is slightly off when compared to the measured signal propagation time (in the experimental case) or the forward stepping time (in the numerical case). In addition one can see that in the numerical case the peak is more spread-out

than in the experimental case, which can be explained by the fact that in the numerical case we start from a slightly smeared load distribution in order to avoid the numerical noise associated with concentrated forces, while the experiment takes the actual point impact into account.

We wish to investigate the effect of the location and number of the sensors on the performance of the source identification procedure. This is done for the data obtained numerically, for which we define two separate tests in which we change the positions of the sensors from those specified above. The sensors remain on the left boundary throughout the tests. To make the sensor positions in the tests clear, we add a system of coordinates at the bottom left corner of the plate, so that the sensors are positioned along the y coordinate.

In the first test we use three sensors at each stage of the test, where the distance between position 1 and position 2, and also between position 2 and position 3 is always 0.04 m, (see Fig. 12, where the y axis was rotated into a horizontal position). The positions of the sensors coincide with the nodes of the mesh.

We plot the cost of the refocused solution as a function of y_1 , which is the y coordinate of the sensor position 1—see Fig. 14a. The horizontal dashed line in that figure is a somewhat arbitrary line above which there are multiple peaks that may interfere with the identification of the true refocused peak.

The cost of the obtained solution varies depending on the precise location of the sensor on the boundary, but most of this boundary produces good identification. This would suggest

Fig. 12 Example of sensor positions in first test

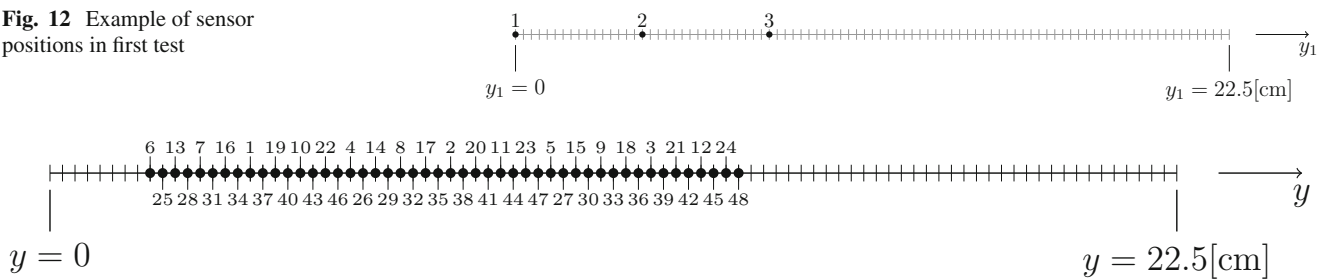
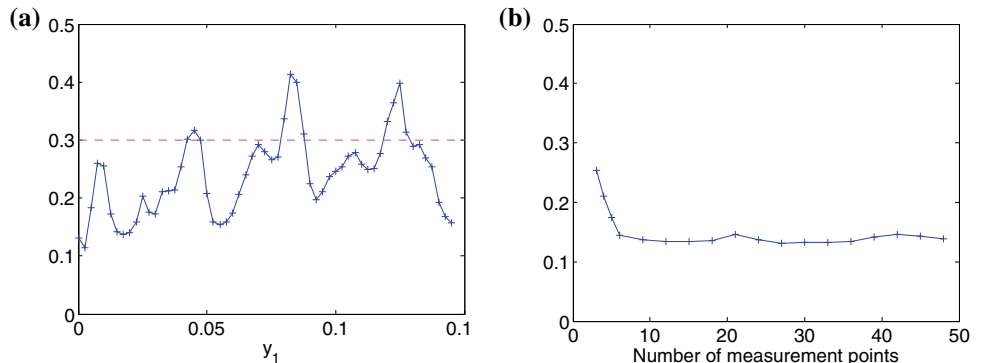


Fig. 13 Example of sensor positions in second test

Fig. 14 Sensor positions on left boundary: **a** Cost versus position of lowest sensor; **b** Cost versus number of sensors in the same area



moving the sensors slightly if at first the identification is not good.

In a second test, we check the dependence of the cost on the number of sensors, which are placed at the same region on the left boundary. The sensor positions still coincide with the mesh, and up to 48 measurement points are used in the different stages of the test. The order by which the sensors are added is shown in Fig. 13, and the cost vs. the number of measurement points is shown in Fig. 14b. One may note that at different stages of the test 3 sensors are added together to the measurement setup.

Figure 14b shows that when the number of sensors is increased beyond 6 in the interval [2, 14], no gain in identification is obtained. However, identification may be improved by placing additional sensors at those locations which are most favorable (see Fig. 14a). Since those locations are not known a priori, one may place many sensors along the boundary to guarantee sufficient contribution to the refocusing.

As our results above show, the three sensors of Configuration are sufficient to achieve refocusing in the particular case considered.

5 Flaw Identification: An Example

5.1 The Numerical Models

In the case of the flaw (hole) identification example we seek to identify the location of a square hole that is made in the

plate, using a known impact source and the data from the three sensors. In these experiments we use the aluminum plate. We therefore construct numerical models of Configurations 2 and 3 listed in Table 1, again considering a domain with the dimensions given in Fig. 3. Each of the configurations was modeled with the associated corresponding geometry—the model of Configuration 2 is simply a rectangle with the corresponding external dimensions, and in the model of Configuration 3 we use the same rectangle, but we introduce a square hole, albeit with sharp corners instead of the rounded ones that exist in the physical model.

Each configuration was again meshed with a structured mesh of square elements with a side length of 2.5 mm. Thus, the mesh of Configuration 2 contains 13,950 elements, while the mesh of Configuration 3 contains 13,550 elements. The hole in Configuration 3 is modeled in such a manner that it replaces whole elements and does not require any adaptation of the mesh. We do not carry out any mesh refinement in the vicinity of the corners of the hole; however, as shown below, this does not render the matching procedure between the signal obtained from the physical plate with the hole and the signal from the discrete numerical model invalid, even with the increased error in the numerical signal that is obtained with the sharp corners. The location of the sensors in this experiment was slightly different with Position 1 at (0, 0.05 m), Position 2 at (0, 0.075 m) and Position 3 at (0, 0.1 m). The sensors measure the x -displacements.

We now introduce a square hole in the plate model, which coincides with the square hole in the experimental Configu-

ration 3. The hole does not cross the mesh lines. The location of the hole is chosen so that it lies between the source and the sensors, i.e. the upper left corner of the square hole is located at (0.0875, 0.15). The side length of the square of the hole is 5 cm.

In other respects that do not concern the square hole and the sensors the mesh and model of the experiment are similar to those used for the source identification example.

We note that we assume from the outset that the crack is aligned with the mesh lines. This is not a limitation of our TR identification methodology, but rather a limitation of our discretization method, which is based on a standard FE formulation and standard elements. It is appropriate to use a more general discretization method which allows for scatterers that cut into element interiors, e.g., an inclined crack, or a crack whose tip reaches inside an element. Two methods that accomplish this are XFEM [34–37] and embedded boundary methods, also called immersed boundary methods or fictitious domain methods; see, e.g., [38]. In the context of cracks, the XFEM has the additional advantage that the crack-tip singularity can easily be incorporated in the functional basis. A totally different approach, which also allows flexibility of the damage location with respect to the mesh, is based on an adjoint formulation; see [39].

5.2 The Cost and the Identification Process

In the process of searching for the best candidate flaw, which produces the best cost (see below) as a measure of identification we only search for flaws of the same shape and size as the true hole, which may be positioned at different locations throughout the plate model. Due to the requirement that the hole coincides with an element boundary in the mesh it is possible to scan all permitted locations of the candidate holes in the model mesh (permitted locations are such that the candidate hole does not penetrate the perimeter boundary of the plate). Thus we do not perform an optimization on the hole location space, but rather search it exhaustively.

The identification process consists of the following. For a given plate model with a hole with unknown location we produce a forward run for $N = 600$ time steps and obtain the displacement readings at the sensors, as in the source identification case. We then assume that we do not know the location of the hole and guess that location. We perform a time-reversed run and obtain the solution field at the time step $N = 600$, which is equivalent to the time of the ball's impact.

In considering the cost devised previously for the source identification, see (26), we find that it is no longer adequate in the flaw identification setting, mostly due to the fact that in the former case the location of the cost is not known, while in the latter it is known and one can utilize the distance metric between the true and refocused sources to judge the quality

of identification, a “good” solution field should be a one for which the guessed hole is close to the true one. The other components of the cost remain those listed in (26), with the changes listed below that were introduced.

One change made in the cost function for hole identification is the fact that we use the energy field, $E(\mathbf{w}) = \frac{1}{2}[\rho\dot{w}_i\dot{w}_i + \check{\sigma}_{ij}\check{\epsilon}_{ij}]$ as the field in which we expect refocusing to occur. This is not a mandatory choice, but rather a choice made due to the quality of identification in each particular case, which may vary from one problem to another. We use here the same components of the cost as in the source identification case, namely the total variation and the average of the solution field, where the former is now defined as

$$TV = \frac{1}{N_{np}} \sum_A \sqrt{E_{,x}^2 + E_{,y}^2}, \quad (27)$$

and the latter is taken outside of a square containing the largest peak. However, in addition to these we now also use the distance of the maximum in the refocused field from the known location of the source. All of these components of the cost are calculated, in the present case, with respect to the energy field.

The other change made in the cost function with respect to the case of (26) is the addition of the following technique to get rid of all the wave paths between the sensors and the refocused source that have nothing to do with the obstacle: We make one TR run without the obstacle at all. Therefore, in the TR without the obstacle we get at reversed time $\tau = T$ a solution that we shall call \mathbf{w}_0 , whose energy is $E(\mathbf{w}_0)$. As seen from Fig. 15, $E(\mathbf{w}_0)$, at least in the present Configuration 3, exhibits refocusing even though the obstacle is missing. Now, each subsequent TR run with another guess for the location of the obstacle will produce a solution \mathbf{w} at $\tau = T$, from which we shall calculate $\mathbf{w}' = \mathbf{w} - \mathbf{w}_0$, and will apply the score to $E(\mathbf{w}')$ rather than to $E(\mathbf{w})$.

The cost function contains components which depend on the calculated solution field $\mathbf{w}(\tau = 600)$, and others which depend on the difference of this displacement field from the reference displacement field described above. We denote the difference field by $\mathbf{w}^{diff}(\tau = 600)$, and the energy associated with that difference by E^{diff} . Thus, the cost we employ will be of the form:

$$\begin{aligned} Cost_H = & K_0 \frac{av(E(\Omega_{out}))}{max(E(\Omega))} + K_1 \frac{av(E^{diff}(\Omega_{out}))}{max(E(\Omega))} \\ & + K_2 \frac{TV(E(\Omega_{out}))}{max(E(\Omega))} + K_3 \frac{dist(E^{diff}(\Omega))}{L}. \end{aligned} \quad (28)$$

Here, K_0 to K_3 are constants; Ω_{out} is the domain of the problem which lies outside the square Ω_R which contains the peak (we did not want to include the peak in the calculated average

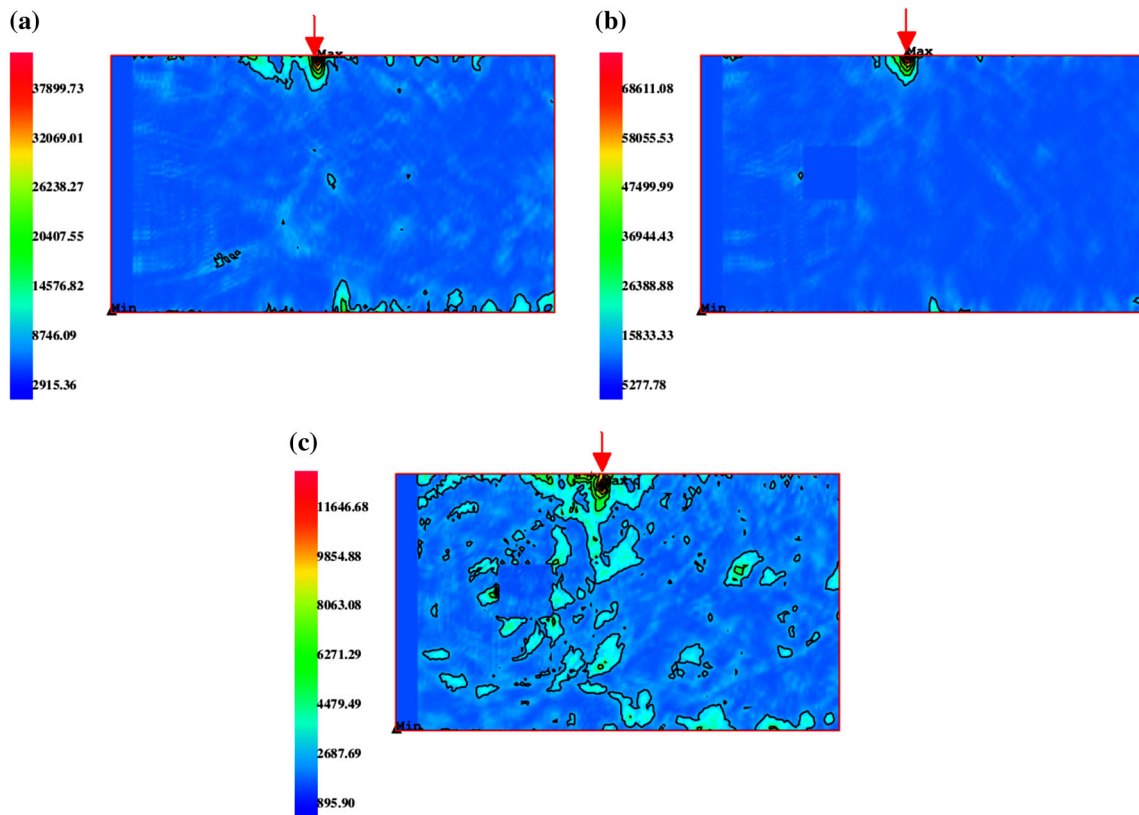


Fig. 15 Refocusing in energy field using signal numerically synthesized in the presence of 5 cm hole: **a** no hole in TR run; **b** with 5 cm hole at the true location in TR run; **c** energy of the difference between the displacements $w - w_0$ in **a**, **b**

field—just the outside “ripples”). Also here the operator av stands for the average of the field (E or E^{diff}), max stands for the maximum of this field, $dist$ is the distance between the maximum of the respective field (E^{diff}) and the location of the impact source, and L is the length of the plate.

In principle, there is no reason to base the cost function, and therefore the identification procedure, on a single property of the field at the reverse time $\tau = T$. In fact in [30] the cost function contained components based on the displacement as well as components based on the energy. In a sense, the E and E^{diff} fields that appear in (28) are such different fields—one which removes waves that do not come in contact with the flaw and one that does not. Since the former may spoil other aspects of the refocused field, it may be beneficial in some cases (as our suggested cost function reflects) to use either or both fields in the cost.

In the calculations below we used the constants: $K_0 = 8$, $K_1 = 8$, $K_2 = 0.0025$, $K_3 = 3$. Again, these are not optimal constants, but rather constants which were found to give good identification results (see the results shown below). Other constants may be found that also give identification results—the performance is not very sensitive to the precise numbers chosen. However, the constants are problem-specific, and would have to be tuned for a problem with different geometry.

5.3 Hole Identification Trials

Before carrying out the hole identification process we carry out a calibration procedure (see Sect. 4.3) on the aluminum plate which does not contain a hole (Configuration 2) in order to obtain the properties of this material, as used in the subsequent forward and time-reversed runs. For Configuration 2 (aluminum) the optimized values obtained were $\bar{\mu} = 25.9$ GPa, $\bar{\lambda} = 50.2$ GPa, and the corresponding plane stress values of $\mu = 25.9$ GPa, $\lambda = 25.5$ GPa. These values were also used in the identification runs performed with Configuration 3.

We obtain measurement signals at the three sensor positions from a forward numerical run and from the experimental setup. For the latter we tune the linear transformation parameters that complete the calibration procedure described in Sect. 4.3. We then scan the space of hole locations, and for each of these locations we perform a time-reversed run, and assign the appropriate cost to the solution.

Figures 16 and 17 show the respective performance of the TR procedure with these two types of sensor signals. The abscissas of the graphs Figs. 16a and 17a scan the numbers of the nodes in the identification mesh at which the bottom left corner of the hole is located. Since the mesh in numbered

Fig. 16 Energy field-based cost in hole identification test with numerically synthesized data: **a** mode number view; **b** distance view

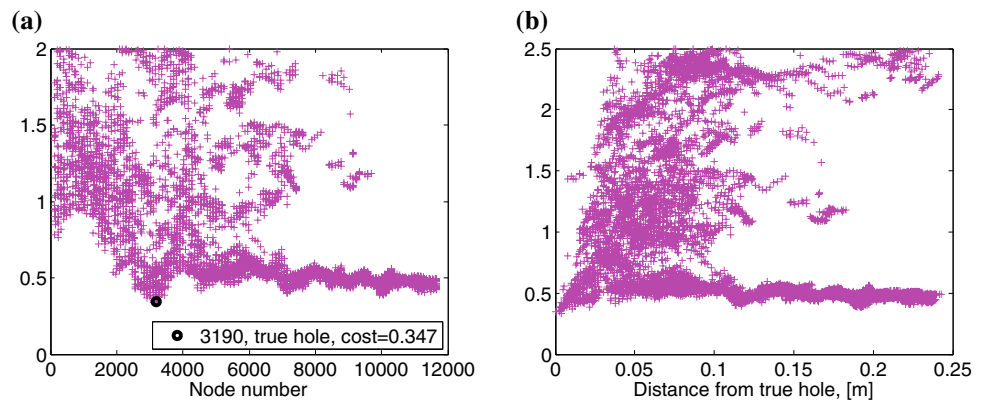
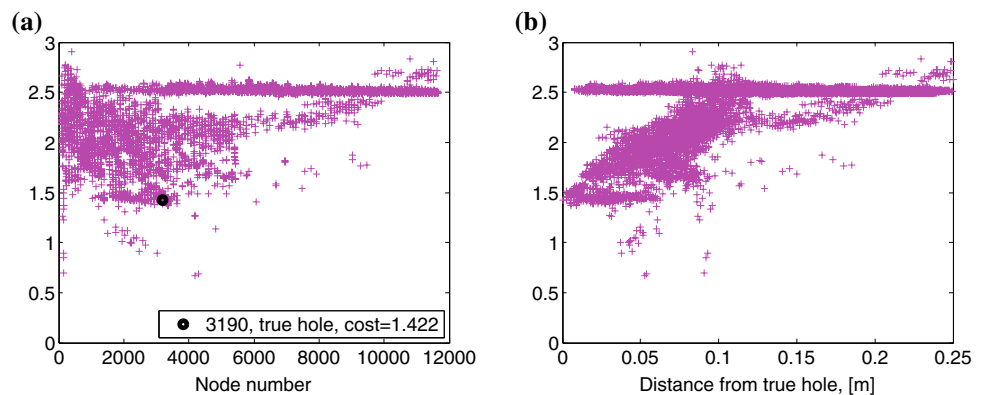


Fig. 17 Energy field-based cost in hole identification test with experimental data: **a** mode number view; **b** distance view



first along the vertical direction upwards from the bottom left corner of the plate, and then to the right along the long dimension of the plate, increasing node numbers generally corresponds to locations that are more to the right along the plate.

The abscissas of the graphs Figs. 16b and 17b scan the distances between the candidate holes and the true hole while the ordinates are the same as in Figs. 16a and 17a, respectively. Good performance is expected to be reflected on Figs. 16b and 17b by flaws close to the true one giving low costs and flaws farther away giving higher costs. This of course assumes that the true hole is known, which is only true for performance tests such as the one done here—such graphs cannot be plotted when the true hole is not sought and has to be found.

One can see from Fig. 16 that when the sensor data input is taken from the numerical forward problem, the identification scheme succeeds in identifying the true hole, which is assigned the lowest cost of all the candidate holes searched. It should be noted, however, that in this case there is a large number of false holes which are assigned good costs (though higher than the best cost of the true solution) lying to the right of the true hole.

On the other hand, when the sensor data is taken from the experiment, the identification scheme does not perform well—there are many false positive solutions which despite

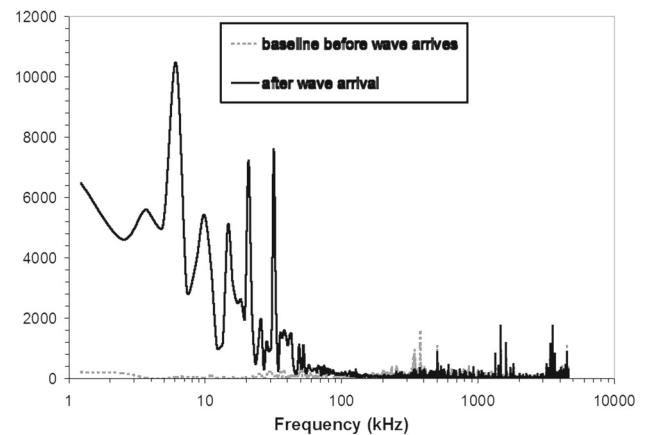


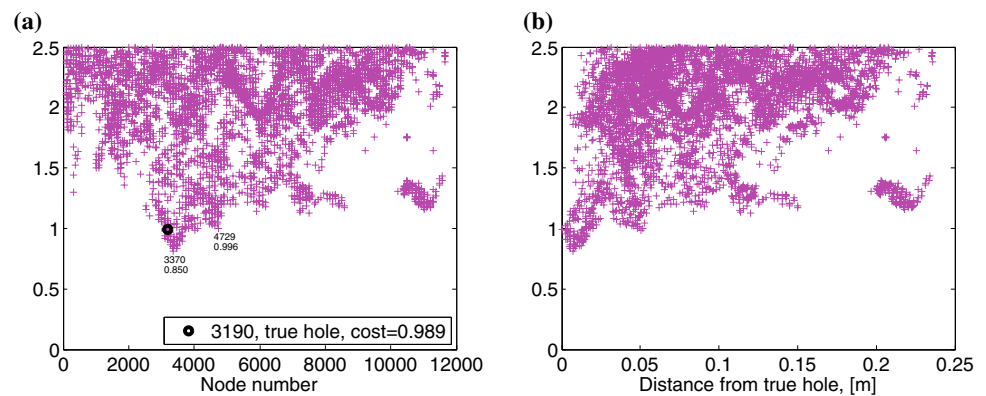
Fig. 18 Frequency spectrum of the experimental data signal

the lower cost they receive, lie far away from the true hole. This situation, however, can be improved upon by filtering the experimental signal:

We perform filtering by performing FFT analysis of the data signal. The frequency content of the signal is shown in Fig. 18, together with the baseline signal in which no impact has occurred yet.

It is evident that at frequencies higher than about 100 kHz both datasets are quite similar, and if one wants to filter out only the hardware noise, this frequency should be the

Fig. 19 Energy field-based cost in hole identification test with filtered experimental data: **a** mode number view; **b** distance view



cutoff threshold. However, we found that it is sufficient to perform the cutoff at much lower frequencies—the largest peak in Fig. 18 occurs at about 6 kHz, and although the range $6 \div 100$ kHz contains a lot of the signal's energy, the main contribution to the shape of the waveform occurs at the lower end of this range. It was therefore decided to remove all but the 1000 lowest frequencies in the FFT plot (the 1000-th frequency corresponds approximately to 6 kHz).

Subsequently, we apply inverse FFT analysis, and the resulting signal is used as the new (filtered) sensor data signal. Fig. 19 shows the performance of the TR procedure with the filtered sensor signals.

The true hole does not receive in this case the lowest cost, rather—the lowest cost is that of the hole whose bottom left corner is at node 3370 (whose cost is 0.850), as shown in the figures. But this node is only two elements away from the true hole, and in fact, all the “+” marks which have a cost lower than that of the true hole are very close to it. The best hole away from the true hole has its bottom left corner at node 4729, and receives a cost higher than the true one.

In any case, the holes with the lowest costs lie very near the true hole, and there is no “tail” of false holes with good costs in this case, therefore the filtered case even surpasses the performance of the case with the numerically synthesized data.

6 Concluding Remarks

In this paper we have shown how the TR technique can be used, with lab acquired data, to identify sources (passive identification) or flaws (active identification) in structures. To guarantee success in the identification, certain special procedures must be taken, as was described. The results shown here demonstrate that TR has the potential to serve as a viable model-based NDT technique, providing much more information on the damage than conventional NDT. However, the technique relies on costly optimization, and is therefore not yet a practical tool for industrial purposes.

Recently, Amitt et al. [40] proposed to combine Arrival Time Imaging and TR in order to greatly accelerate the identification process, by significantly reducing the search space for the TR. This and additional ideas, related to model reduction, may prove useful in making the technique an efficient and practical NDT procedure to be used by the industry.

Acknowledgements The work of D.G. was partly supported by the fund provided through the Lawrence and Marie Feldman Chair in Engineering.

References

- Schmerr, L.W., Song, J.S.: *Ultrasonic Nondestructive Evaluation Systems: Models and Measurements*. Springer, Berlin (2007)
- Drinkwater, B.W., Wilcox, P.D.: Ultrasonic arrays for non-destructive evaluation: a review. *Nondestruct. Test. Eval. Int.* **39**, 525–541 (2006)
- Wall, M., Burch, S.F., Lilley, J.: Review of models and simulators for NDT reliability (POD). *Insight* **51**, 612–619 (2009)
- Kirsch, A.: *An Introduction to the Mathematical Theory of Inverse Problems*, 2nd edn. Springer, Berlin (2011)
- Vogel, C.R.: *Computational Methods for Inverse Problems*. SIAM, Philadelphia (2002)
- Stavroulakis, G.E.: *Inverse and Crack Identification Problems in Engineering Mechanics*. Kluwer, Dordrecht (2001)
- Liu, G.R., Han, X.: *Computational Inverse Techniques in Nondestructive Evaluation*. CRC Press, London (2003)
- Ali, A.S., Nikolova, N.K., Sangary, N.T.: Near-field microwave non-destructive testing for defect shape and material identification. *Nondestruct. Test. Eval.* **21**, 79–93 (2006)
- Kalogeropoulos, A., van der Kruk, J., Hügenschmidt, J., Bikowski, J., Bruhwiler, E.: Full-waveform GPR inversion to assess chloride gradients in concrete. *Nondestruct. Test. Eval. Int.* **57**, 74–84 (2013)
- Goenezen, S., Barbone, P.E., Oberai, A.A.: Solution of the nonlinear elasticity imaging inverse problem: the incompressible case. *Comput. Methods Appl. Mech. Eng.* **200**(13–16), 1406–1420 (2011)
- Hicken, J.E., Li, J., Sahni, O., Oberai, A.A.: Adjoint consistency analysis of residual-based variational multiscale methods. *J. Comput. Phys.* **255**, 396–406 (2013)
- Cho, Y.: Model-based guided wave NDE: the evolution of guided wave NDE from ‘Magic’ to physically based engineering tool. *J. Nondestruct. Eval.* **31**, 324–338 (2012)

13. Starek, L., Inman, D.J.: Design of nonproportional damped systems via symmetric positive inverse problems. *ASME J. Vib. Acoust.* **126**, 212–219 (2004)
14. Allison, T.C., Miller, A.K., Inman, D.J.: A time-varying identification method for mixed response measurements. *J. Sound Vib.* **319**, 850–868 (2009)
15. Erturk, A., Inman, D.J.: Parameter identification and optimization in piezoelectric energy harvesting: analytical relations, asymptotic analysis and experimental validations. *IMEchE J. Syst. Control Eng.* **225**, 485–496 (2011)
16. Seher, M., Huthwaite, P., Lowe, M.J.S., Michael, P.B.: Model-based design of low frequency lamb wave EMATs for mode selectivity. *J. Nondestruct. Eval.* **34**, 22-1–22-16 (2015)
17. Chang, Y.F., Ton, R.C.: Kirchhoff migration of ultrasonic images. *Mater. Eval.* **59**, 413–417 (2001)
18. Hoegh, K., Khazanovich, L., Ferraro, C., Clayton, D.: Ultrasonic linear array validation via concrete test blocks. In: 41st Annual Review of Progress in Quantitative Nondestructive Evaluation, Vol. 34, pp. 83–93 (2015)
19. Grohmann, M., Niederleithinger, E., Buske, S.: Geometry determination of a foundation slab using the ultrasonic echo technique and geophysical migration methods. *J. Nondestruct. Eval.* **35**, 17-1–17-13 (2016)
20. Fink, M., Wu, F., Cassereau, D., Mallart, R.: Imaging through inhomogeneous media using time reversal mirrors. *Ultrason. Imaging* **13**, 179–199 (1991)
21. Givoli, D.: Time reversal as a computational tool in acoustics and elastodynamics. *J. Comput. Acoust.* **22**, 1430001-1–1430001-40 (2014)
22. Derveaux, G., Papanicolaou, G., Tsogka, C.: Time reversal imaging for sensor networks with optimal compensation in time. *J. Acoust. Soc. Am.* **121**, 2071–2085 (2007)
23. Zumpano, G., Meo, M.: A new nonlinear elastic time reversal acoustic method for the identification and localisation of stress corrosion cracking in welded plate-like structures—a simulation study. *Int. J. Solids Struct.* **44**, 3666–3684 (2007)
24. Buerkle, A., Sarabandi, K.: Non-destructive evaluation of elastic targets using acousto-electromagnetic wave interaction and time reversal focusing. *IEEE Trans. Antennas Propag.* **57**, 3628–3637 (2009)
25. Bavu, E., Berry, A.: High-resolution imaging of sound sources in free field using a numerical time-reversal sink. *Acta Acust. United Acust.* **95**, 595–606 (2009)
26. Reyes-Rodriguez, S., Lei, N., Crowgey, B., Udpa, L., Udpa, S.S.: Time reversal and microwave techniques for solving inverse problem in non-destructive evaluation. *Nondestruct. Test. Eval. Int.* **62**, 106–114 (2014)
27. Fan, C.G., Pan, M.C., Luo, F.L., Drinkwater, B.W.: Multi-frequency time-reversal-based imaging for ultrasonic nondestructive evaluation using full matrix capture. *IEEE Trans Ultrason. Ferroelectr. Freq. Control* **61**, 2067–2074 (2014)
28. Givoli, D., Turkel, E.: Time reversal with partial information for wave refocusing and scatterer identification. *Comput. Methods Appl. Mech. Eng.* **213–216**, 223–242 (2012)
29. Levi, I., Turkel, E., Givoli, D.: Time reversal for elastic wave refocusing and scatterer location recovery. *J. Comput. Acoust.* **23**, 1450013-1–1450013-29 (2015)
30. Amitt, E., Givoli, D., Turkel, E.: Time reversal for crack identification. *Comput. Mech.* **54**, 443–459 (2014)
31. Hughes, T.J.R.: *The Finite Element Method*. Prentice Hall, Englewood Cliffs (1987)
32. Bal, G., Ryzhik, L.: Time reversal and refocusing in random media. *SIAM J. Appl. Math.* **63**, 1475–1498 (2003)
33. Treiber, M.A.: *Optimization for Computer Vision*. Springer, London (2013)
34. Rabinovich, D., Givoli, D., Vigdergauz, S.: Crack identification by ‘arrival time’ using XFEM and a genetic algorithm. *Int. J. Numer. Methods Eng.* **77**, 337–359 (2009)
35. Sun, H., Waisman, H., Betti, R.: Nondestructive identification of multiple flaws using XFEM and a topologically adapting artificial bee colony algorithm. *Int. J. Numer. Methods Eng.* **95**(10), 871–900 (2013)
36. Sun, H., Waisman, H., Betti, R.: A multiscale flaw detection algorithm based on XFEM. *Int. J. Numer. Methods Eng.* **100**(7), 477–503 (2014)
37. Sun, H., Waisman, H., Betti, R.: A sweeping window method for detection of flaws using an explicit dynamic XFEM and absorbing boundary layers. *Int. J. Numer. Methods Eng.* **105**, 1014–1040 (2016)
38. Schillinger, D., Rank, E.: An unfitted hp-adaptive finite element method based on hierarchical B-splines for interface problems of complex geometry. *Comput. Methods Appl. Mech. Eng.* **200**, 47–48 (2011)
39. Seidl, R., Rank, E.: Iterative time reversal based flaw identification. *Comput. Math. Appl.* **72**, 879–892 (2016)
40. Amitt, E., Givoli, D., Turkel, E.: Combined arrival-time imaging and time reversal for scatterer identification. *Comput. Methods Appl. Mech. Eng.* **313**, 279–302 (2017)